Journal of Materials Chemistry A

ROYAL SOCIETY OF CHEMISTRY

PAPER

View Article Online
View Journal | View Issue

Cite this: *J. Mater. Chem. A*, 2021, **9**, 7575

Synergetic effects of electrochemical oxidation of Spiro-OMeTAD and Li^+ ion migration for improving the performance of n–i–p type perovskite solar cells†

Changzeng Ding,[ab] Rong Huang,[c] Christian Ahläng,[d] Jian Lin,[b] Lianping Zhang,[b] Dongyu Zhang,[b] Qun Luo,[ab] Fangsen Li,[c] Ronald Österbacka*[bd] and Chang-Qi Ma*[abc]

Received 24th December 2020
Accepted 15th February 2021

DOI: 10.1039/d0ta12458c

rsc.li/materials-a

n–i–p Type perovskite solar cells generally require air oxidation of the Spiro-OMeTAD layer to achieve high power conversion efficiency (PCE). However, the detailed oxidation mechanism is still not fully understood. In this paper, oxidation of Spiro-OMeTAD was demonstrated *via* a non-contact electrochemical route using UV-Vis absorption, laser beam induced current (LBIC) imaging and secondary ion mass spectrometry (SIMS) profiling of the Spiro-OMeTAD films. At the cathode, oxygen is reduced to form OH^- with the help of H_2O, while the anodic reaction is the oxidation of Spiro-OMeTAD to form Spiro-OMeTAD$^+$. Diffusion of Li^+ towards the surface of the Ag electrode completes the electrochemical cycle and increases the conductivity of the hole-transporting layer. SIMS analyses of the completed devices demonstrate that the oxidation of Spiro-OMeTAD also leads to migration of Li^+ through the perovskite layer into SnO_2, which supposedly leads to an increase of the built-in voltage. We verify these results by incorporation of the experimentally measured Li^+ concentration into a numerical drift-diffusion simulation, to replicate solar cell *J*–*V*-curves. This work provides a new insight into the oxidation of Spiro-OMeTAD in perovskite solar cells, and demonstrates that Li^+ migration is involved in the oxidation of Spiro-OMeTAD.

Introduction

Organic–inorganic hybrid perovskite solar cells (PSCs) have recently drawn unprecedented attention due to their high efficiency and low-cost solution processing compatibility.[1–3] Over the last decade, both n–i–p and p–i–n type cells have been reported in the literature.[4–7] In n–i–p type cells, Spiro-OMeTAD doped with Li-TFSI and *t*-BP is generally used as the hole transporting layer (HTL).[8,9] Oxidation of the cells in an ambient atmosphere results in higher device performance.[10–13] Mobility of Spiro-OMeTAD is low ($\sim 4 \times 10^{-5}$ cm^2 V^{-1} s^{-1}), implying slow charge extraction through the undoped Spiro-OMeTAD HTL.[14,15] It is widely accepted that oxidation of the Spiro-OMeTAD layer leads to increased conductivity, which consequently improves the device performance.[16–18] Based on the above speculation, pre-oxidized Spiro-OMeTAD species, including Co(III) complexes,[19,20] Zn-TFSI$_2$,[21,22] CuSCN (or CuI),[23] 2,3,5,6-tetrafluoro-7,7,8,8-tetracyanoquinodimethane (F4-TCNQ),[24] and Spiro(TFSI)$_2$ (ref. 25 and 26), were used as replacements for Li-TFSI doped Spiro-OMeTAD in perovskite solar cells, and consistently good device performance can be achieved for those cells without further oxidation in air.

The oxidation mechanism of Spiro-OMeTAD, however, is not yet fully understood. Bach *et al.* studied the synergetic effect of light soaking and air oxidation of Spiro-OMeTAD in solid-state dye-sensitized solar cells.[10] By comparing the concentration of Spiro-OMeTAD$^+$, determined from UV-vis absorption spectra, oxidation of Spiro-OMeTAD by O_2^- at the TiO_2 surface under light illumination was proposed (Scheme S1 in the ESI†). Snaith *et al.* proposed that molecular oxygen is weakly bound to Spiro-OMeTAD to form a donor–acceptor complex.[27] Under light illumination or thermal excitation, intermolecular electron transfer between Spiro-OMeTAD and O_2 leads to the formation of Spiro-OMeTAD$^+O_2^-$. This electron transfer process is promoted by doping with Li-TFSI, yielding Spiro-OMeTAD$^+$TFSI$^-$ and lithium oxides (Scheme S2 in the ESI†).

[a]*School of Nano-Tech and Nano-Bionics, University of Science and Technology of China, 398 Jinzhai Road, Hefei, 230026, P. R. China*

[b]*Printable Electronic Research Center, Suzhou Institute of Nano-Tec and Nano-Bionics, Chinese Academy of Sciences (CAS), 398 Ruoshui Road, SEID, SIP, Suzhou 215123, P. R. China*

[c]*Vacuum Interconnected Nanotech Workstation, Suzhou Institute of Nano-Tec and Nano-Bionics, Chinese Academy of Sciences (CAS), 398 Ruoshui Road, SEID, SIP, Suzhou 215123, P. R. China*

[d]*Physics and Center for Functional Materials, Faculty of Science and Technology, Åbo Akademi University, Porthaninkatu 3, 20500 Turku, Finland. E-mail: Ronald.Osterbacka@abo.fi*

† Electronic supplementary information (ESI) available. See DOI: 10.1039/d0ta12458c

Although Spiro-OMeTAD does not absorb light of 450 nm wavelength, Meng *et al.* demonstrated that photo-oxidation of Spiro-OMeTAD by oxygen happened when samples were illuminated under light of 450 nm wavelength.[11] Therefore, an oxidation mechanism involving perovskite was proposed as seen in Scheme S3 (ESI†). Qi *et al.* recently compared the influence of O_2 and/or H_2O exposure on photo-electronic spectroscopy and conductivity of Spiro-OMeTAD film.[17] They concluded that H_2O induced an irreversible conductivity enhancement of Spiro-OMeTAD film mainly ascribed to the redistribution of Li-TFSI within the film, while the O_2 induced reversible conductivity enhancement is mainly due to an O_2 doping effect. It is worth pointing out that most of the oxidation mechanism studies were done on model devices where no metal electrode is included. However, the routine oxidation process during solar cell fabrication was performed on a completed cell,[12,28,29] where the Spiro-OMeTAD layer is physically separated from oxygen and/or moisture by a thermally evaporated metal electrode. A full study of the oxidation process after depositing a metal electrode is still lacking in the literature. Understanding the oxidation mechanism of the Spiro-OMeTAD layer in a complete cell is therefore of great interest. In this paper, we found that oxidation of the Spiro-OMeTAD layer is ascribed to an electrochemical oxidation process, where oxygen is reduced to OH^- with the help of water and Spiro-OMeTAD is oxidized to Spiro-OMeTAD$^+$ simultaneously. In addition, we found that the oxidation process is accompanied by migration of Li^+ ions through the perovskite layer and into SnO_2. The synergetic effects of the oxidation process and the Li^+ ion migration on the electronic structures of interlayers, as well as the photovoltaic performance enhancement of the cells will be discussed in detail to give a comprehensive understanding of the oxidation mechanism of the Spiro-OMeTAD layer and consequences for device performance. This paper provides a new understanding of the oxidation process and the associated Li^+ ion migration in n–i–p type perovskite solar cells.

Experimental

Materials

The SnO_2 colloid solution was purchased from Alfa Aesar (tin(IV) oxide, 15 wt% in H_2O colloidal dispersion). PbI_2, $PbBr_2$, CsI, formamidinium iodide (FAI), methylammonium bromide (MABr), lithium bis(trifluoromethanesulphony)imide (Li-TFSI), pyridine,4-(1,1-dimethylethyl)- (*t*-BP) and Spiro-OMeTAD were purchased from Xi'an Polymer Light Technology Corp. Poly(3,4-ethylenedioxythiophene):poly(styrene sulfonate) (PEDOT:PSS AI 4083) was purchased from Heraeus Precious Metals GmbH & Co. KG. CsI was purchased from Sigma-Aldrich, and dimethylformamide (DMF, purity > 99%), dimethyl sulfoxide (DMSO, purity > 99%), and chlorobenzene (CB, purity > 99%) were purchased from J&K Scientific.

Instruments and characterization

The current density–voltage (*J*–*V*) characteristics of the solar cells were measured with a Keithley 2400 source meter in a N_2 glovebox under simulated sunlight (AM 1.5G, Newport VeraSol-2 LED Class AAA Solar Simulator). Time-of-flight secondary ion mass spectrometry (TOF-SIMS 5-100) was performed with pulsed primary ions from a Cs^+ (2 keV) liquid-metal ion gun for sputtering and a Bi^+ pulsed primary ion beam for analysis (30 keV). The absorption curves of the sample were analysed using a UV-visible spectrometer (Lambda 750, PerkinElmer). Laser beam induced current (LBIC) and photoluminescence (PL) of the solar cells under different oxidation conditions were tested using a home-built defect imaging system (LBIC). The PL maps were collected using a laser with a wavelength of 532 nm, and a scan step of 40 μm.

Preparation of the perovskite precursor and Spiro-OMeTAD solution

The $FA_{0.85}MA_{0.15}Pb(I_{0.85}Br_{0.15})_3$ precursor solution (named FAMA) was prepared by dissolving PbI_2 (548.6 mg), $PbBr_2$ (77.07 mg), FAI (190.12 mg), and MABr (21.84 mg) in a solvent mixture of DMF/DMSO (1 mL, 4 : 1 v/v). Then, 34 μL CsI (2 M in DMSO) was added to the FAMA mixed perovskite solution to obtain the CsFAMA tri-cation perovskite precursor solution. The Spiro-OMeTAD solution was prepared by dissolving 72.3 mg Spiro-OMeTAD into 1 mL chlorobenzene followed by the addition of 17.5 μL Li-TFSI (520 mg mL^{-1} in acetonitrile) and 29 μL *t*-BP.

Solar cell fabrication

ITO glass was cleaned by ultrasonic cleaning with detergent, pure water, acetone, and isopropanol for 30 min, respectively. Before use, the ITO substrate was dried in a N_2 gas flow, and cleaned by UV–ozone treatment for 30 min. Then the substrate was spin-coated with a thin layer of SnO_2 nanoparticles from the SnO_2 colloid solution at 3000 rpm for 30 s, and annealed in ambient air at 150 °C for 30 min. After cooling down to room temperature, 40 μL CsFAMA solution was spin-coated onto SnO_2 at 5000 rpm for 30 s, and 200 μL anti-solvent of ethyl acetate was dropped 10 seconds before the end of the spin-coating process. The films were then annealed at 120 °C for 45 min. After being cooled down to room temperature, Spiro-OMeTAD solution was spin-coated on the corresponding mixed perovskite films at 3000 rpm for 30 s. Finally, 100 nm of silver was evaporated on the top of Spiro-OMeTAD as the back electrode to complete the whole device.

Oxidation of Spiro-OMeTAD films and complete solar cells

In general, oxidation of the Spiro-OMeTAD films, the hole only devices and the complete solar cells was performed inside a glovebox with controlled relative humidity for a certain time. The glovebox was covered with aluminium foil to ensure dark conditions. The reference cell with Spiro-OMeTAD was completed by thermal evaporation of the top electrode directly after the deposition of the Spiro-OMeTAD layer. For the pre-oxidized device, the half-cell with the Spiro-OMeTAD layer was kept inside the atmosphere-controlled glovebox in the dark for 5 hours before the deposition of the top electrode, while the post-oxidation process was carried out by putting the complete device with the top metal electrode inside the same glovebox in the dark for the given amount of time.

Preparation of Spiro-OMeTAD films for UV-vis absorption measurement

The glass substrate was cleaned by the same procedure as for the ITO glass. Glass/Spiro-OMeTAD films were prepared by depositing Spiro-OMeTAD on glass at 3000 rpm for 30 s. Glass/SnO_2/Spiro-OMeTAD was prepared by depositing SnO_2 by the same procedure as for solar cell fabrication, followed by depositing Spiro-OMeTAD on SnO_2 films at 3000 rpm for 30 s. The UV-vis spectrum of the Spiro-OMeTAD film was measured using a spectrometer, and the oxidation process was performed in the atmosphere (with RH ~30%) within the spectrometer to make sure that there is no position variation during the measurement.

Preparation of hole only devices

The PEDOT:PSS (1 mL PEDOT:PSS solution in 2 mL deionized water) solution was spin-coated on the top of the cleaned ITO at 2000 rpm for 45 s and then annealed at 130 °C for 10 min in air. After cooling down, 35 μL Spiro-OMeTAD solutions with different doping concentrations were spin-coated on the corresponding PEDOT:PSS films at 3000 rpm for 30 s inside a N_2 glovebox. Finally, 100 nm of silver was evaporated on the top of Spiro-OMeTAD as the back electrode.

Results and discussion

J–V characteristics of n–i–p cells under oxidation in 30% RH air

Fig. 1a shows the perovskite solar cell structure adopted in this study, where Li-TFSI/*t*-BP doped Spiro-OMeTAD (Li-TFSI:Spiro-OMeTAD, 50%, mol mol^{-1}) and SnO_2 are used as the hole transporting layer (HTL) and the electron transporting layer (ETL), respectively. To ensure a good reproducibility of the oxidation of the Spiro-OMeTAD layer, we conducted the oxidation processes in the dark in a synthesized air atmosphere with 30% relative humidity (30% RH). Fig. 1b shows the variation of the current density–voltage (*J–V*) curves for the complete cells oxidized in 30% RH air for different periods of time, with corresponding photovoltaic data listed in Table 1. Surprisingly, the freshly prepared device showed almost no photovoltaic performance without oxidation processes. We checked the *J–V* of several freshly prepared cells with pristine Spiro-OMeTAD, and they all showed very poor photovoltaic performance (see statistical data in Fig. S1 in the ESI†). This can be ascribed to the low conductivity of the pristine Spiro-OMeTAD film (*vide infra*). After exposure to the 30% RH air for 1 hour, the cell showed an improved PCE of 3.19% with an open-circuit voltage (V_{oc}) of 0.97 V, a short-circuit current (J_{sc}) of 11.47 mA cm^{-2}, and a fill factor (FF) of 0.29. The performance of the cells was further improved to 11.66%, 14.18%, and 18.72% after oxidation for 2, 3 and 5 hours in the dark (see full statistical data in Fig. S1†). Note that no significant *J–V* performance improvement was found for the cells after several rounds of *J–V* sweeping under light illumination (see examples in Fig. S2†). Since the cells were kept in the dark in 30% RH air in between the *J–V* measurements during oxidation, we ascribed the device performance enhancement to the oxidation process, rather than the bias or light illumination effect during *J–V* sweeping. Interestingly, oxidation of the cells mostly leads to the enhancement of J_{sc} in the first 2 hours, followed by improvement of the FF in the later oxidation stage (Table 1), which is ascribed to the decrease of the charge injection barrier and

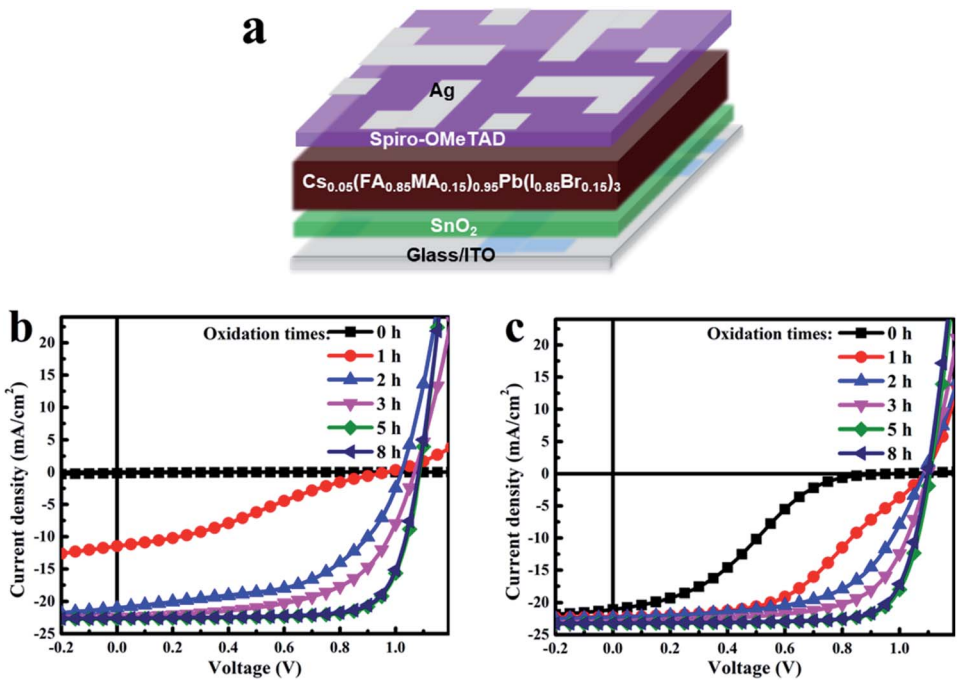

Fig. 1 (a) Solar cell configuration adopted in this study; (b and c) current density–voltage (*J–V*) curves of completed perovskite solar cells with the as-prepared (b) and pre-oxidized (5 hours, (c)) Spiro-OMeTAD hole transporting layers exposed to 30% RH air.

Table 1 The photovoltaic performance data of the perovskite solar cells exposed to 30% RH air for different periods of time

Pre-oxidation time[a] (h)	Post-oxidation time[b] (h)	V_{oc} (V)	J_{sc} (mA cm^{-2})	FF	PCE (%)
0	0	0.68	0.16	0.13	0.01
	1	0.97	11.47	0.29	3.19
	2	1.02	21.00	0.54	11.66
	3	1.06	22.44	0.59	14.18
	5	1.08	22.65	0.76	18.72
	8	1.08	22.58	0.76	18.51
5	0	0.97	21.08	0.28	5.83
	1	1.08	22.23	0.48	11.60
	2	1.08	22.29	0.59	14.34
	3	1.10	23.17	0.65	16.52
	5	1.11	23.23	0.77	19.71
	8	1.10	23.20	0.77	19.52

[a] Time for keeping the ITO/SnO_2/PVSK/Spiro-OMeTAD in 30% RH air. [b] Time for keeping the complete cell in 30% RH air.

consequently the series resistance as supported by the simulation results (*vide supra*). Further increase of the oxidation time, however, showed a saturation effect of the oxidation process (Table 1 and Fig. S2 in the ESI†).

To distinguish the influence of oxygen and water in the oxidation process on device performance, we compared the device performance enhancement of cells oxidized in a N_2 atmosphere with 30% and 50% relative humidity (RH), and in an air atmosphere with RH = 30% and dry air. Fig. S3† shows the results. As seen here, device performance improved much slower in dry air than in a moisture containing atmosphere. These results indicate that water plays an important role in rapidly improving the device photovoltaic performance. Oxygen was also reported to be important for the performance improvement in perovskite solar cells.[18,27] The comparison of the photovoltaic performance enhancement rates of the cells oxidized in 30% RH air and 30% N_2 confirmed that oxygen is able to promote the oxidation processes (Fig. S3†). Therefore, we concluded that both oxygen and water can oxidize the Spiro-OMeTAD layer.

According to the literature,[18,27,30] oxidation of Spiro-OMeTAD will lead to the formation of Spiro-OMeTAD$^+$, increasing the conductivity of the Spiro-OMeTAD layer. We also prepared a glass/Spiro-OMeTAD (50% LiTFSI, *t*-BP) film and exposed it to 30% RH air. Fig. S4 in the ESI† shows the UV-Vis absorption spectra of this film with increasing exposure time. An increased absorbance over 450–600 nm can be seen, which is ascribed to the formation of Spiro-OMeTAD$^+$,[27] confirming that Spiro-OMeTAD can be effectively oxidized when directly exposed to 30% RH air. We then fabricated n–i–p type solar cells with a pre-oxidized Spiro-OMeTAD layer (before the deposition of the Ag top electrode, the incomplete device was exposed to 30% RH air in the dark for 5 hours) and checked the device performance of this type of cell. Fig. 1c shows the *J–V* curves of a representative cell under AM 1.5G light illumination. As seen here, the as-prepared cell with the pre-oxidized Spiro-OMeTAD cell showed an S-shaped *J–V* curve with a V_{oc} of 0.97 V, a J_{sc} of 21.08 mA cm^{-2}, an FF of 0.28, and an overall PCE of 5.83% (Fig. 1c, black-squared line). It is worth noting that we found that oxidation of the half cells under light illumination will result in much better device performance (Fig. S5†), which might be the reason for the difference in initial device performance after pre-oxidation to reported results.[31] In comparison with the cell without pre-oxidation (Fig. 1b, black-squared line), the cell that underwent the pre-oxidation process indeed showed improved device performance, mainly in terms of V_{oc} and J_{sc}. However, this cell showed a low FF of 0.28, indicating that charge extraction is far from satisfactory. Further oxidation of this cell in 30% RH air (named the post-oxidation process) improved the device performance (Fig. 1c and Table 1), which was mainly due to the increase of FF. Eventually, a champion device with V_{oc}, J_{sc}, and FF of 1.11 V, 23.23 mA cm^{-2}, and 0.77 was obtained after oxidation in air for 5 hours, yielding an overall PCE of 19.71%, which is comparable with the reported performance for the cell without modification on the SnO_2 layer.[28,32–34] Statistical data are shown in Fig. S6.† These results indicate that, in addition to the improved conductivity of the Spiro-OMeTAD upon oxidation, some other indirect improvement to charge extraction, such as an increase in the built-in voltage, may take place in the pre-oxidized sample.

LBIC images of the cells during oxidation

To confirm whether the 100 nm Ag electrode can effectively block the diffusion of H_2O and/or O_2, we checked the water vapor transmission rate (WVTR) of PET (125 μm) foils with different Ag thin films (50–200 nm). The WVTR was measured to be 22, 62, and 370 mg per m^2 per day in a 100% RH atmosphere for PET with 200, 100 and 50 nm Ag films. The WVTR of the PET/Ag films is much lower than that of PTE foil (2200 mg per m^2 per day, see ESI Fig. S7†), suggesting that 100 nm Ag is able to slow down the penetration of water and oxygen through the Ag electrode in the present experiment (few hours in 30% RH air). We also checked the influence of Ag layer thickness on the performance enhancement of the cells under identical oxidation conditions. As seen in Fig. S8,† there is no obvious difference in the performance improvement rate upon oxidation when the thickness of the Ag electrode is increased from 50 nm to 200 nm. In addition, we checked the PL mapping of a large area perovskite solar cell (1.21 cm^2) during oxidation, and a homogeneous decrease of the PL intensity over 8 hours of oxidation was measured with a simultaneous slow increase of device performance (Fig. S9 in the ESI†). Both results indicated that the oxidation of Spiro-OMeTAD should not be due to the penetration of oxygen/water through the Ag film, since diffusion of oxygen/water requires a longer time with the increase of Ag layer thickness and device area. So, if the oxidation of Spiro-OMeTAD required the direct contact of Spiro-OMeTAD with the oxidant, the only pathway for the oxidation process is penetration of oxygen (and/or water) through the edge of the metal electrode. To confirm whether edge penetration is the path for the oxidation process, we measured the homogeneity of the photocurrent of the cells during oxidation using the laser beam induced current (LBIC) imaging method. Fig. 2 shows the

LBIC images of a representative cell oxidized for different periods of time. As seen here, for the freshly prepared cell, there is almost no photocurrent over the whole cell area, which is in good accordance with the low measured J_{sc} of 0.16 mA cm^{-2} (Table 1). The increased current for the cell with increased oxidation time corresponds very well to the *J–V* results (Fig. 1b and Table 1). Importantly, we found that the increase of photocurrent is spatially homogeneous over the active cell area, confirming that the oxidation of Spiro-OMeTAD is probably through a non-contact route, since otherwise a gradient improvement from the edge to the centre of the cell would be observed. Meanwhile, in order to study the impact of light on the device performance during the LBIC test, we compared the *J–V* curves of the cell before and after the LBIC test, and no significant performance enhancement was measured for the cells (Fig. S10†), confirming that light illumination is not the main reason for the device performance enhancement.

Li^+ ion migration and proposed electrochemical oxidation of Spiro-OMeTAD

To gain a deep insight into the oxidation process of the Spiro-OMeTAD film, we conducted time-of-flight secondary-ion mass spectrometry (TOF-SIMS)[35,36] on a model device with a structure of ITO/Spiro-OMeTAD (50% Li-TFSI:*t*-BP doping)/Ag. Fig. S4b in the ESI† shows the UV-Vis absorption spectra of this device upon air exposure. Increased absorption over 450–600 nm can also be detected, indicating that oxidation of the Spiro-OMeTAD happens in this device as well. Fig. 3a shows elemental profiles of Li, F and LiOH within the devices, before and after oxidation. Although $TFSI^-$ (as determined from the distribution of F element) is almost homogeneously distributed over the Spiro-OMeTAD layer, higher Li concentrations were measured at the Ag/Spiro-OMeTAD and Spiro-OMeTAD/ITO interfaces even for the freshly prepared sample. This result indicates that Li^+ is not compatible with the Spiro-OMeTAD films, which can be ascribed to the different hydrophilicities of Li^+ and Spiro-OMeTAD molecules. Pre-oxidation of the Spiro-OMeTAD film further increased the Li^+ concentrations at the Ag/Spiro-OMeTAD and Spiro-OMeTAD/ITO interfaces (Fig. 3a, red lines), indicating migration of Li^+ ions towards the two electrodes during the oxidation process. Qi *et al.* also reported the accumulation of Li^+ at the Spiro-OMeTAD surface and ascribed it to the formation of LiOH during oxidation of Spiro-OMeTAD in air.[16,17] Additionally, oxidation of the device with the pre-oxidized Spiro-OMeTAD film (post-oxidation process) further increased the Li^+ and LiOH concentrations at the Ag/Spiro-OMeTAD interface, with a decrease of Li^+ concentration within the Spiro-OMeTAD layer (Fig. 3a, blue lines), indicating that the post-oxidation process further promotes Li^+ ion migration. More importantly, high Li^+ and LiOH concentrations were measured on the silver electrode surface (see Fig. S11† for the distribution of Li^+ in a 3D manner). These results indicate that Li^+ ions can diffuse through the Ag electrode to reach the surface, which can be ascribed to the relatively high OH^- concentration at the Ag electrode surface originating from the reduction of O_2/H_2O. To summarize these observations, electrochemical oxidation of Spiro-OMeTAD is suggested as shown in Scheme 1. The cathodic reaction is the reduction of water and oxygen to form OH^- (eqn (1) in Scheme 1), while the anodic oxidation reaction is the oxidation of Spiro-OMeTAD to form Spiro-OMeTAD$^+$ (eqn (2) in Scheme 1). The diffusion of Li^+ towards the surface of the Ag electrode completes the electrochemical cycle. The overall oxidation reaction is summarized in eqn (3), similar to that reported in the literature.[11,27] Note that no significant performance decrease was measured for the optimized cell after storage in the dark in a N_2 glovebox (Fig. S12†), which confirms that the oxidation process is not reversible.

Ion migration within the complete perovskite solar cell

Fig. 3b depicts the measured Li, F ($TFSI^-$), and LiOH distributions in the complete device before and after oxidation. Surprisingly, a very high Li concentration was detected within the SnO_2 layer, even for the freshly prepared device (Fig. 3b, black line). A similar profile was also measured for LiOH but with two orders of magnitude lower intensity. We also checked the elemental distribution of glass/ITO/SnO_2/PVSK films, and no Li was detected at the perovskite/SnO_2 interface (Fig. S13 in

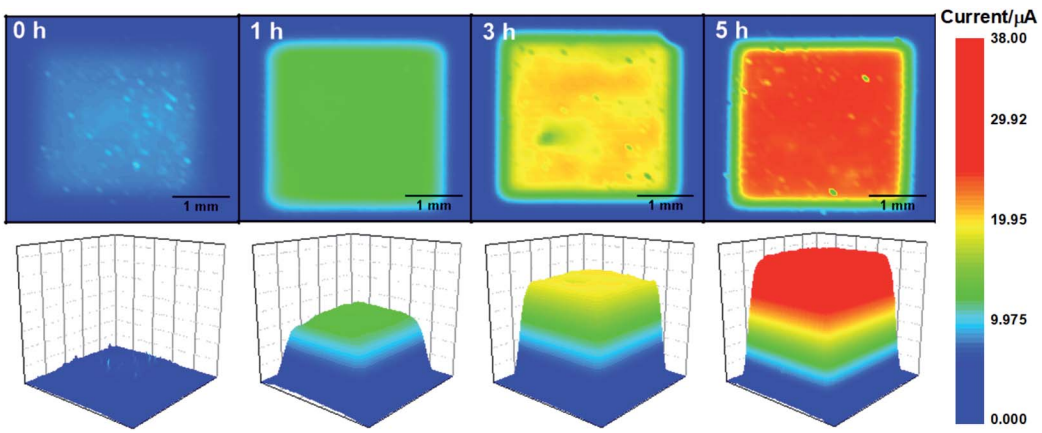

Fig. 2 LBIC images of the perovskite solar cell aged in 30% RH air for different periods of time.

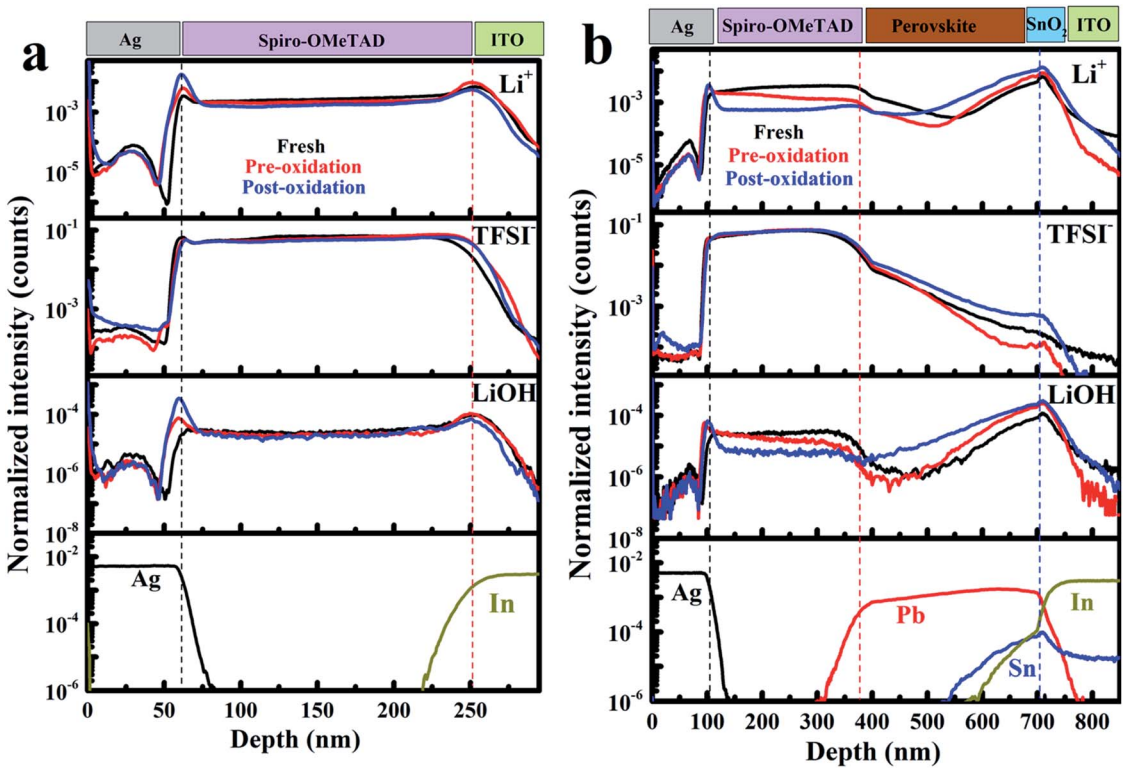

Fig. 3 (a) Elemental depth profile of the ITO/Spiro-OMeTAD/Ag films (a) and complete perovskite solar cell with a structure of ITO/perovskite/Spiro-OMeTAD/Ag (b) with different oxidation treatments. Note that the ion intensity is in the logarithmic scale.

the ESI†). These results indicate that in the complete perovskite solar cell, the measured high Li concentration at the perovskite/SnO_2 interface must come from the Spiro-OMeTAD layer. In other words, Li^+ ions can migrate from the Spiro-OMeTAD layer through the perovskite film to the SnO_2 layer during the preparation of the solar cell. This finding is in agreement with Zhu *et al.*[37] who reported that Li^+ ions could diffuse into the TiO_2 during the preparation of perovskite solar cells. However, they drew this conclusion based on the high F signals measured within the TiO_2 layer.[37] Here, we use TOF-SIMS to directly measure the distribution of Li atoms, providing solid evidence for the Li^+ ion migration into the SnO_2 layer. It is worth noting that no significant performance improvement was measured for a cell upon multiple *J–V* sweeps (Fig. S2†), indicating that the bias applied to the cell during the *J–V* sweeping should not be the driving force for Li^+ migration. It was reported that doping the TiO_2 electron extraction layer with an alkali salt is also able to improve device performance.[38] SIMS analysis showed a high concentration of K^+ in the SnO_2 layer for the prepared cell (Fig. S13 in the ESI†), similar to that reported in the literature.[28,29,39,40] Interestingly, diffusion of K^+ from SnO_2 to the perovskite layer can be clearly seen for the freshly prepared

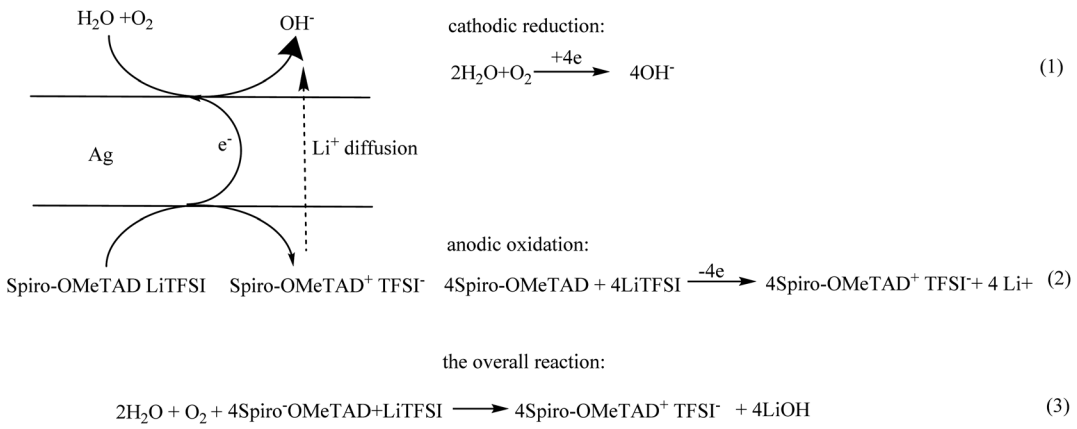

Scheme 1 Proposed electrochemical oxidation of Spiro-OMeTAD.

perovskite cell. Further migration of K^+ ions into the Spiro-OMeTAD layer occurs upon oxidation treatment (see Fig. S13b†). Since SnO_2 has been considered as an excellent cathode material for lithium batteries because of its high Li^+ affinity,[41] we considered the high Li^+ affinity of SnO_2 to be the driving force for the Li^+ ion migration. In the meanwhile, the diffusion of K^+ into the Spiro-OMeTAD layer provides an ion balance within the cell, which is believed to be another important driving force for the diffusion of Li^+ ions.

Fig. S4c† shows the UV-Vis absorption change of the Li-TFSI doped Spiro-OMeTAD films deposited on the SnO_2 layer upon 30% RH air exposure, and Fig. S4d† shows the comparison of UV-Vis absorption enhancement over 450–600 nm. As seen here, SnO_2 promotes the formation of Spiro-OMeTAD$^+$, which can probably be ascribed to the fact that the diffusion of Li^+ ions into the SnO_2 layer lowers the cation concentration within Spiro-OMeTAD and consequently promotes the oxidation process. It is also worth noting that $TFSI^-$ did not diffuse into the SnO_2 layer, probably due to the large molecular size of $TFSI^-$, since F element was mainly measured within the Spiro-OMeTAD layer with a long tail over the perovskite film.

In the cell with the pre-oxidized Spiro-OMeTAD film, increased Li concentration was found in the SnO_2 layer. Accordingly, the Li concentration in the Spiro-OMeTAD layer near the Spiro-OMeTAD/perovskite interface is decreased, indicating that more Li^+ ions close to the Spiro-OMeTAD/perovskite interface diffused into the SnO_2 layer during the pre-oxidation process. In comparison with the freshly prepared cell, we measured a similar Li concentration in the Spiro-OMeTAD film near the Ag/Spiro-OMeTAD interface but with a slightly increased Li concentration at the Ag/Spiro-OMeTAD interface for the pre-oxidized cell. These results indicate that oxidation of the ITO/SnO_2/perovskite/Spiro-OMeTAD film can cause a relatively high Li^+ concentration at the Spiro-OMeTAD surface, corresponding well to the pre-oxidized Spiro-OMeTAD only film (*vide supra*). Furthermore, oxidation also drives the Li^+ ions from the Spiro-OMeTAD/perovskite interface to migrate into the SnO_2 layer.

For the post-oxidized cell, we measured more Li^+ diffusing into the SnO_2 layer from the Spiro-OMeTAD layer. However, we also measured higher concentrations of Li and LiOH at the Ag/Spiro-OMeTAD interface. This result indicates that post-oxidation of Spiro-OMeTAD also drives Li^+ ion diffusion into SnO_2. The distribution of F element, however, does not change during oxidation, suggesting that $TFSI^-$ is rather stable within the Spiro-OMeTAD film, which could be due to the relatively large molecular dimensions as well. The SIMS result of the complete cell upon oxidation demonstrated that oxidation of the complete cell in air, on the one hand, leads to the formation of Spiro-OMeTAD$^+$, and also promotes Li^+ diffusion through the perovskite to the perovskite/SnO_2 interface. Knowing the ion migration behaviors of the n–i–p perovskite solar cells upon oxidation, we then studied the influence of LiTFSI doping concentration on the oxidation processes. To simplify the study, we only compared the influence of LiTFSI doping concentration on the post-oxidation process. The results are shown in Fig. S14.† As seen there, when the LiTFSI doping ratio is lower than 50%, the perovskite solar cells showed poor device performance with low FF of 0.30–0.45, similar to that of a 50% LiTFSI doped cell (*vide infra*). With the increase of oxidation time, the device performance is gradually improved. Also, with a higher LiTFSI doping concentration, the cell showed slightly faster performance improvement and better saturated device performance. When the LiTFSI doping ratio is increased to 70%, the device showed an initial PCE of 14.75% with an FF of 0.69. However, instead of further performance improvement, a slight decrease of PCE was found for this cell upon further oxidation. These results indicate that Li^+ concentration within the Spiro-OMeTAD layer plays an important role in determining the device performance and stability.

Influence of the oxidation process on charge extraction of the Spiro-OMeTAD layer

Fig. S15† shows the *J–V* curves of the hole only devices with a structure of ITO/PEDOT:PSS/Spiro-OMeTAD (undoped or 50% LiTFSI:*t*-BP doped)/Ag exposed to a 30% RH atmosphere. As seen here, an over three orders of magnitude increase of the current density was measured for the doped device upon oxidation (Fig. S15a†), which can be ascribed to the increased conductivity of the Spiro-OMeTAD layer.[25,27,42,43] In contrast, for the undoped device, the measured current injected from the Ag side stays low ($\sim$0.01 mA cm^{-2} at a bias of 5 V) and roughly the same upon oxidation (Fig. S15b†), suggesting that Li-TFSI doping can promote the oxidation of Spiro-OMeTAD, similar to what was reported by Snaith *et al.*[27]

Fig. 4a shows the UV photoelectron spectroscopy (UPS) spectra of the Spiro-OMeTAD films with or without oxidation. Together with the UV-Vis absorption spectra of the Spiro-OMeTAD (Fig. S4†), we estimated the HOMO/LUMO energy levels of the fresh and oxidized Spiro-OMeTAD films to be $-4.96/-2.06$ eV and $-5.02/-2.81$ eV, respectively. As seen here, the LUMO energy levels of Spiro-OMeTAD are lower by 0.77 eV after oxidation, due to the formation of Spiro-OMeTAD$^+$. However, the HOMO energy level shifts only 0.08 eV after oxidation. A similar trend was also reported by Qi *et al.*[16] And we expect that the HOMO energy will change only slightly after the post-oxidation process. The energy levels of the materials used in this work are shown in Fig. 4b.

The influence of the ion distribution on the *J–V* characteristics of the solar cells was further clarified using numerical simulations using a drift-diffusion model.[44] The simulation parameters are found in Table S1 in the ESI.† We modelled the oxidation of the Spiro-OMeTAD layer at a uniform p-type doping concentration ranging from undoped to 5×10^{18} cm^{-3}, shown in Fig. 4c and d. Here, we assumed that the SnO_2 layer is ideal to single out the effect of the increasing doping concentration. The device with an undoped Spiro-OMeTAD layer shows essentially no photovoltaic effect, but as the doping concentration increases, large J_{sc} and V_{oc} are obtained first, followed by a steady improvement in the FF. The simulation results are similar to those of the as-prepared device, suggesting that the primary effect of the oxidation is the increased doping concentration in the Spiro-OMeTAD layer. However, the slight S-shape observed in the as-prepared sample 1 h after fabrication was not reproduced. In the pre-oxidized sample, the S-shape is

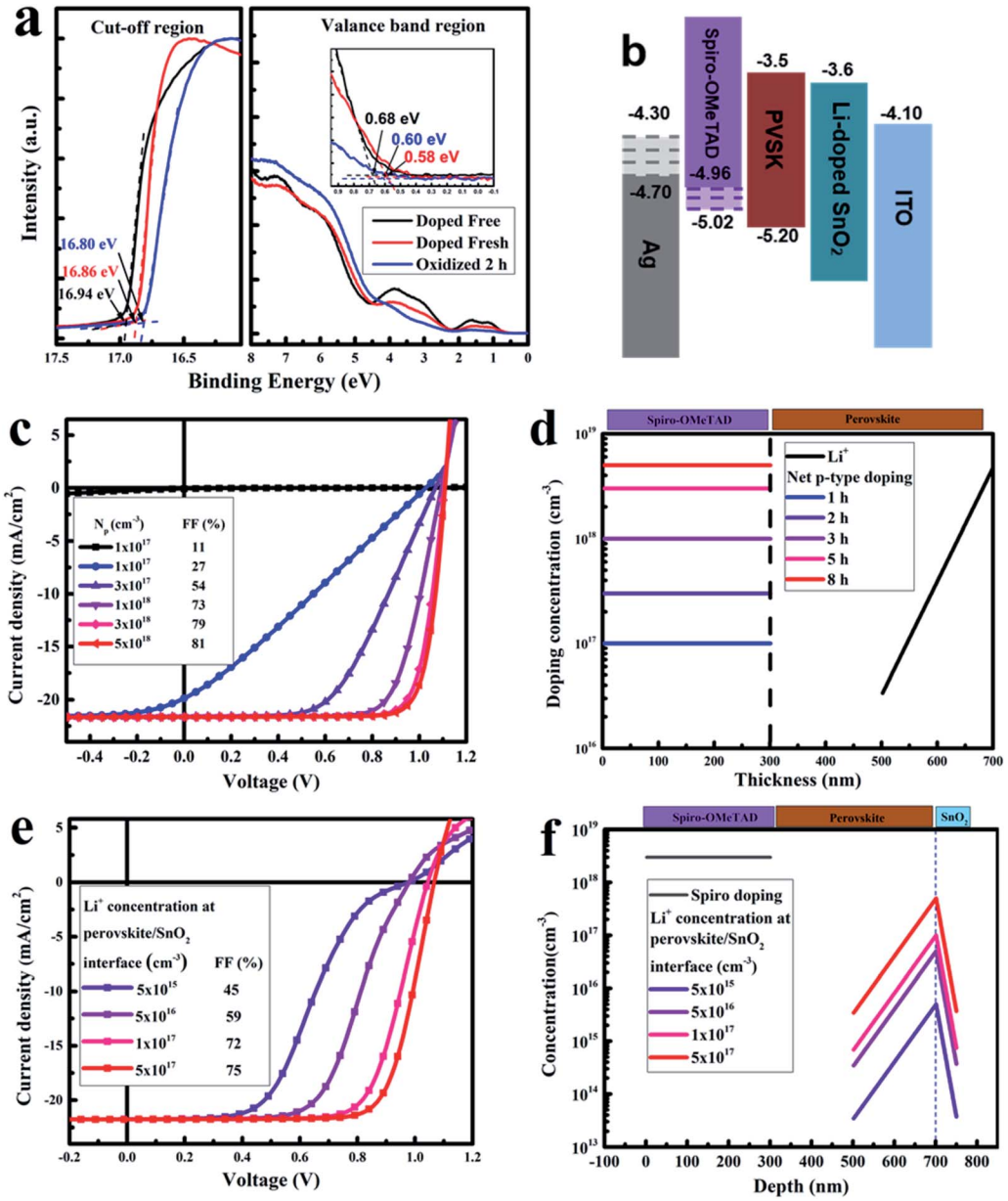

Fig. 4 (a) UPS spectra for the Spiro-OMeTAD films upon oxidation. The left part of each spectrum is the secondary electron cut-off region, and the right part is the valence band (VB) region. The inset shows the enlarged spectra in the VB region to give the exact distance of the VB to the Fermi energy level. (b) Energy-level scheme for the perovskite solar cell with different interfacial layers. (c) Simulated J–V curves of the cell using a defined Li^+ profile with changing the doping concentration of the Spiro-OMeTAD layer (d). (e) Simulated J–V curves of the cell using a defined doping concentration with the realistic Li^+ ion profile at the PVSK/SnO_2 interface (f).

much more pronounced, and here we would expect that the pre-oxidation of the Spiro-OMeTAD layer has achieved a reasonably large doping concentration. We then fixed the doping concentration in the Spiro-OMeTAD layer at 3×10^{18} cm^{-3} and included the SnO_2 layer in the simulation, using the Li^+ ion distribution obtained from TOF-SIMS (Fig. 3b). Fig. 4e and f show the simulation results for a few different concentrations of Li^+ ions at the perovskite/SnO_2 interface. When the concentration of Li^+ ions is low, the simulated J–V curves exhibit a clear S-shape, similar to that observed in the pre-oxidized sample. As the Li^+ ion concentration increases, the S-shape gradually disappears until a good FF is obtained, and V_{oc} improves slightly. This highlights the importance of the Li^+ ions for the device performance: when we do not assume the SnO_2 layer to be ideal, a build-up of Li^+ ions in the SnO_2 layer is essential to achieve excellent device performance. We also simulated the effect of a change in the work function of the Ag electrode as it becomes oxidized, shown in Fig. S16.† These simulations gave rise to an S-shape but did not resemble the experimental data as closely as the curves with the profile arising from Li^+ diffusion into the SnO_2.

The mechanisms behind the improvements in device performance seen in the simulations are two-fold. Due to the low hole mobility of Spiro-OMeTAD, assumed to be 5×10^{-5}

$cm^2\ V^{-1}\ s^{-1}$ in the simulation, holes cannot travel through the rather thick layer quickly enough. When the layer becomes doped, the conductivity of the layer increases, and at a doping concentration of around $3 \times 10^{18}\ cm^{-3}$, the conductivity is large enough not to limit the device performance, as outlined by Le Corre *et al.*[45] The SnO_2 layer is thin enough and has a high enough mobility not to require doping for efficient extraction of charge,[46] and the improvement in performance due to the build-up of Li^+ can instead be explained in terms of an improved built-in voltage. A low built-in voltage means that the electric field in the device becomes inverted even at small applied voltages and prevents extraction of charge carriers from the perovskite layer, which can result in an S-shape.[45] When the concentration of Li^+ ions at the perovskite/SnO_2 interface is low, the built-in voltage is determined by the difference in work function between the (doped) Spiro-OMeTAD layer and the ITO substrate. When the Li^+ ion concentration in the SnO_2 becomes sufficiently high, the work function of the ITO aligns with that of the (now doped) SnO_2, thus increasing the built-in voltage. In addition, the built-in voltages within the cell with different Li^+ concentrations at the SnO_2 layer were simulated and the results are shown in Fig. S17.† As seen here, with the increase of the Li^+ concentration from $5 \times 10^{15}\ cm^{-3}$ to $5 \times 10^{17}\ cm^{-3}$, the built-in voltage increased gradually from 0.79 V to 1.18 V, in good accordance with the experimental result, where the S-shaped *J–V* curve vanished after oxidation in air for a certain time.

In order to further understand the effect of oxidation process on charge extraction in the full device, photoluminescence (PL) mapping of the fresh, pre-oxidation and post-oxidation solar cells was conducted and the results are shown in Fig. 5a. As seen here, for the fresh cell, the active area shows strong PL intensity, indicating that carriers cannot be effectively extracted by the fresh Spiro-OMeTAD layer. However, the pre-oxidation process decreases the PL intensity for the solar area, which means that the injection efficiency of photongenerated charge carriers to the Spiro-OMeTAD layer was improved. The following post-oxidation process further decreases the PL intensity of the solar cell area (Fig. 5b), which means that the charge carriers can be effectively injected into Spiro-OMeTAD layers. Both pre-oxidation and post-oxidation treatments are beneficial for the extraction of carriers. To quantify this process, time-resolved photoluminescence (TRPL) spectra were collected and fitted to a biexponential decay function. As shown in Fig. 5c and Table S2,† the fresh device shows much higher lifetimes (τ_1 of 22.62 ns, τ_2 of 53.99 ns) than pre-oxidation (τ_1 of 7.46 ns, τ_2 of 35.46 ns) and post-oxidation (τ_1 of 4.77 ns, τ_2 of 29.86 ns) devices. The decreased lifetime also confirmed that the interface contact was enhanced during the oxidation process.

Synergetic effects of oxidation and Li^+ ion migration on the solar cell performance enhancement

Based on the results of the experiments described above, we draw a complete oxidation process of the Spiro-OMeTAD as shown in Fig. 6. We first concluded that electrochemical oxidation of Spiro-OMeTAD happens when a n–i–p type perovskite solar cell is exposed to humid air (Scheme 1). Oxidation of the cell leads to the formation of Spiro-OMeTAD$^+$ (Fig. S4†) and increases the conductivity as seen from the *J–V* curves (Fig. S15†). The (electrochemical) oxidation process also changes the work function of the silver electrode. Both of these

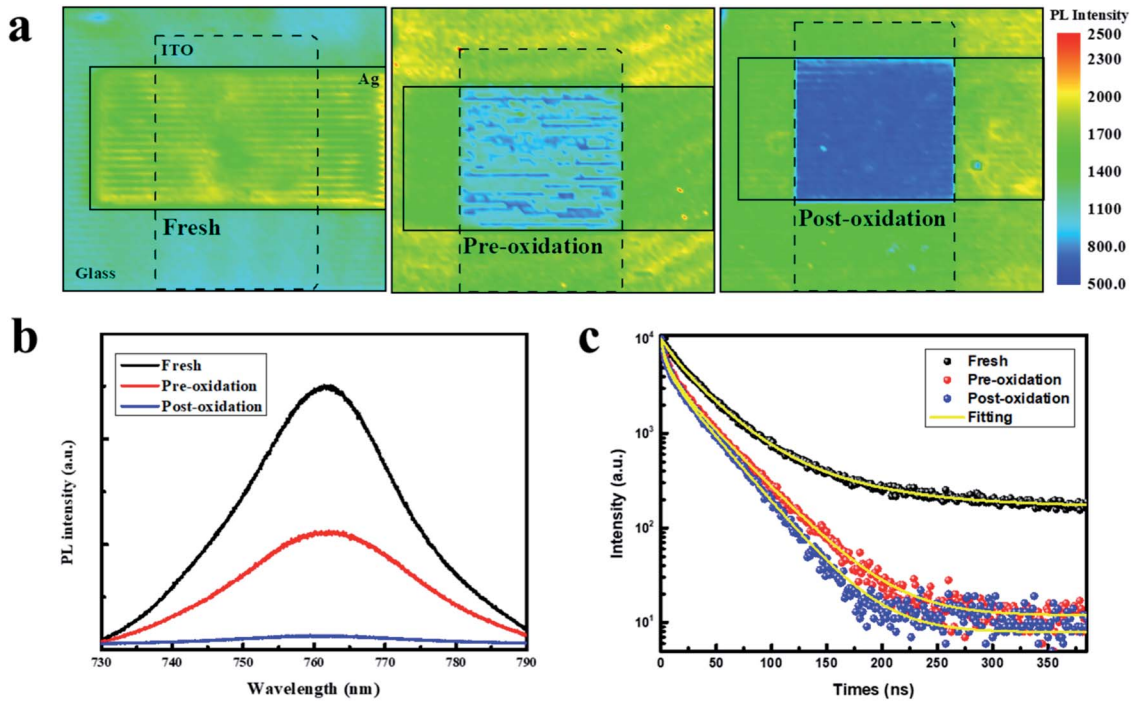

Fig. 5 (a) Photoluminescence (PL) maps of the fresh, pre-oxidation and post-oxidation solar cells. (b) Steady-state PL spectra and (c) time-resolved PL lifetimes of the active area with different oxidation states.

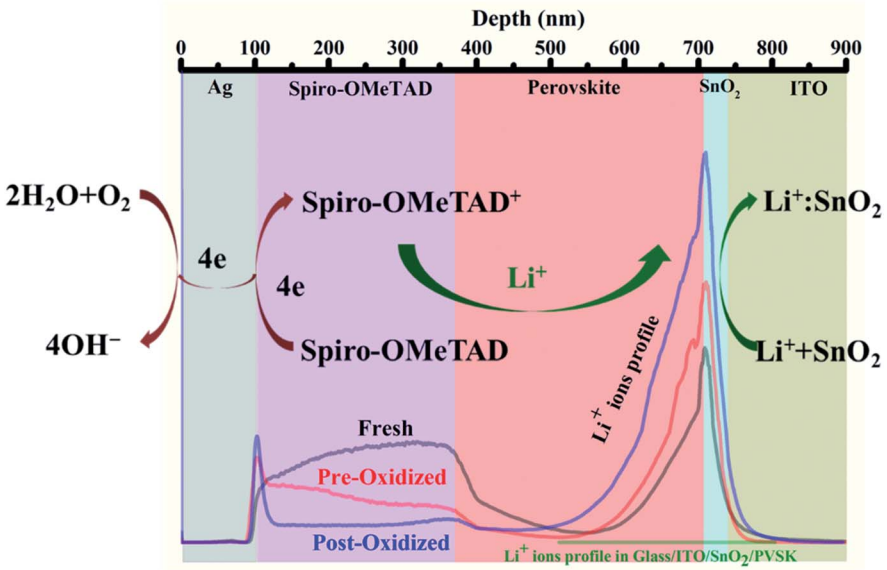

Fig. 6 A complete figure of the oxidation of Spiro-OMeTAD for perovskite solar cells.

effects are favourable for improving the charge extraction through the Spiro-OMeTAD hole-transporting layer (Fig. S15†). SIMS results of the completed cell after oxidation demonstrated that Li^+ ions of the Spiro-OMeTAD layer migrate through the perovskite layer into the SnO_2 layer (Fig. 3b). The diffusion of Li^+ from the Spiro-OMeTAD layer will increase the electron density of the Spiro-OMeTAD layer and further promote the oxidation of Spiro-OMeTAD (Fig. S4d and e†). The concomitant Li^+ diffusion into SnO_2 increases the conductivity, facilitating better device performance (Fig. 4d). Hence, the synergetic effects of Spiro-OMeTAD oxidation and Li^+ ion migration significantly improve the charge transport efficiency and device performance, which explains the necessity of the post-oxidation process of the cells, even when pre-oxidation of the Spiro-OMeTAD was conducted.

Since the performance of the n–i–p type perovskite cells is highly sensitive to the distribution of Li^+ ions within the cell, further oxidation of the cells in ambient air would lead to the accumulation of Li^+ at the SnO_2 layer. Fig. S18a in the ESI† shows the performance evolution of the n–i–p type perovskite solar cells exposed to 30% RH ambient air for a long time. As seen here, the PCE of the cell decreased to 16.89% after oxidation in air for 108 hours, indicating that further diffusion of Li^+ would lead to the decrease of device performance. In other words, Li^+ ion migration is directly related to the stability of the cells.[37] However, our results showed that if we keep the optimized cell in an inert atmosphere, the device performance can be stable for over 240 hours (Fig. S18b†). In other words, the cell performance can be stable if the Li^+ migration can be successfully blocked, which is under investigation by our research group.

Conclusions

In this paper, we conducted a comprehensive study on the oxidation mechanism of the Spiro-OMeTAD layer of n–i–p type perovskite solar cells. By combining the UV-Vis absorption of the Spiro-OMeTAD film, LBIC images of the perovskite solar cells, and elemental distribution of the cells during oxidation, we confirmed that oxidation of the Spiro-OMeTAD layer is carried out through a non-contact electrochemical route. Oxygen and water serve as the oxidant, Spiro-OMeTAD is the reductant, and Li^+ serves as the supporting ion to complete the electrochemical cycle. SIMS analysis of the complete cell demonstrated the Li^+ migration within the cell during oxidation. Such a Li^+ ion migration was found to be able to promote the oxidation of Spiro-OMeTAD and to reduce the LUMO energy level of SnO_2, which simultaneously improve hole and electron extraction at the perovskite/Spiro-OMeTAD and perovskite/SnO_2 interfaces. We could confirm the conclusions drawn from the measurements by reproducing the measured *J–V* curves from the prepared solar cells using numerical simulations where we included the experimentally determined Li^+ ion doping profiles. For the first time, a complete scheme for the oxidation of Spiro-OMeTAD of n–i–p type perovskite solar cells was provided.

Conflicts of interest

There are no conflicts to declare.

Acknowledgements

The authors would like to acknowledge the financial support from the Ministry of Science and Technology of China (No. 2016YFA0200700), Chinese Academy of Sciences (No. YJKYYQ20180029, CAS-ITRI 2019010, and 2020VCA0012), and Jiangsu Science and Technology Program (BX2019111). CA acknowledges funding from the Doctoral Network in Materials Research at Åbo Akademi University and the Swedish Cultural Foundation in Finland. Rö acknowledges the Jane and Aatos Erkko Foundation through the ASPIRE project.

Notes and references

1 A. Kojima, K. Teshima, Y. Shirai and T. Miyasaka, *J. Am. Chem. Soc.*, 2009, **131**, 6050–6051.
2 P. Wang, Y. Wu, B. Cai, Q. Ma, X. Zheng and W.-H. Zhang, *Adv. Funct. Mater.*, 2019, **29**, 1807661.
3 F. Huang, M. Li, P. Siffalovic, G. Cao and J. Tian, *Energy Environ. Sci.*, 2019, **12**, 518–549.
4 S. S. Mali and C. K. Hong, *Nanoscale*, 2016, **8**, 10528–10540.
5 H. Kim, K.-G. Lim and T.-W. Lee, *Energy Environ. Sci.*, 2016, **9**, 12–30.
6 L. Meng, J. You, T.-F. Guo and Y. Yang, *Acc. Chem. Res.*, 2016, **49**, 155–165.
7 A. K. Jena, A. Kulkarni and T. Miyasaka, *Chem. Rev.*, 2019, **119**, 3036–3103.
8 Z. Hawash, L. K. Ono and Y. Qi, *Adv. Mater. Interfaces*, 2018, **5**, 1700623.
9 G.-W. Kim, H. Choi, M. Kim, J. Lee, S. Y. Son and T. Park, *Adv. Energy Mater.*, 2020, **10**, 1903403.
10 U. B. Cappel, T. Daeneke and U. Bach, *Nano Lett.*, 2012, **12**, 4925–4931.
11 S. Wang, W. Yuan and Y. S. Meng, *ACS Appl. Mater. Interfaces*, 2015, **7**, 24791–24798.
12 Q. Jiang, Z. Chu, P. Wang, X. Yang, H. Liu, Y. Wang, Z. Yin, J. Wu, X. Zhang and J. You, *Adv. Mater.*, 2017, **29**, 1703852.
13 I. Jeon, A. Shawky, H.-S. Lin, S. Seo, H. Okada, J.-W. Lee, A. Pal, S. Tan, A. Anisimov, E. I. Kauppinen, Y. Yang, S. Manzhos, S. Maruyama and Y. Matsuo, *J. Am. Chem. Soc.*, 2019, **141**, 16553–16558.
14 T. Leijtens, I.-K. Ding, T. Giovenzana, J. T. Bloking, M. D. McGehee and A. Sellinger, *ACS Nano*, 2012, **6**, 1455–1462.
15 J. Salunke, X. Guo, Z. Lin, J. o. R. Vale, N. R. Candeias, M. Nyman, S. Dahlström, R. O. Sterbacka, A. Priimagi, J. Chang and P. Vivo, *ACS Appl. Energy Mater.*, 2019, **2**, 3021–3027.
16 Z. Hawash, L. K. Ono, S. R. Raga, M. V. Lee and Y. Qi, *Chem. Mater.*, 2015, **27**, 562–569.
17 Z. Hawash, L. K. Ono and Y. Qi, *Adv. Mater. Interfaces*, 2016, **3**, 1600117.
18 Z. Li, J. Tinkham, P. Schulz, M. Yang, D. H. Kim, J. Berry, A. Sellinger and K. Zhu, *Adv. Energy Mater.*, 2017, **7**, 1601451.
19 J. H. Noh, N. J. Jeon, Y. C. Choi, M. K. Nazeeruddin, M. Grätzelb and S. I. Seok, *J. Mater. Chem. A*, 2013, **1**, 11842–11847.
20 J. Burschka, F. Kessler, M. K. Nazeeruddin and a. M. Grätzel, *Chem. Mater.*, 2013, **25**, 2986–2990.
21 J.-Y. Seo, H.-S. Kim, S. Akin, M. Stojanovic, E. Simon, M. Fleischer, A. Hagfeldt, S. M. Zakeeruddin and M. Grätzel, *Energy Environ. Sci.*, 2018, **11**, 2985–2992.
22 Y. Saygili, H.-S. Kim, B. Yang, J. Suo, A. B. Muñoz-Garcia, M. Pavone and A. Hagfeldt, *ACS Energy Lett.*, 2020, **5**, 1271–1277.
23 M. Li, Z.-K. Wang, Y.-G. Yang, Y. Hu, S.-L. Feng, J.-M. Wang, X.-Y. Gao and L.-S. Liao, *Adv. Energy Mater.*, 2016, **6**, 1601156.
24 J. Luo, C. Jia, Z. Wan, F. Han, B. Zhao and R. Wang, *J. Power Sources*, 2017, **342**, 886–895.
25 W. H. Nguyen, C. D. Bailie, E. L. Unger and M. D. McGehee, *J. Am. Chem. Soc.*, 2014, **136**, 10996–11001.
26 B. Tan, S. R. Raga, A. S. R. Chesman, S. O. Fürer, F. Zheng, D. P. McMeekin, L. Jiang, W. Mao, X. Lin, X. Wen, J. Lu, Y.-B. Cheng and U. Bach, *Adv. Energy Mater.*, 2019, **9**, 1901519.
27 A. Abate, T. Leijtens, S. Pathak, J. l. Teuscher, R. Avolio, M. E. Errico, J. Kirkpatrik, J. M. Ball, P. Docampo, I. McPhersonc and H. J. Snaith, *Phys. Chem. Chem. Phys.*, 2013, **15**, 2572–2579.
28 D. Yang, R. Yang, K. Wang, C. Wu, X. Zhu, J. Feng, X. Ren, G. Fang, S. Priya and S. F. Liu, *Nat. Commun.*, 2018, **9**, 3239.
29 T. Bu, X. Liu, Y. Zhou, J. Yi, X. Huang, L. Luo, J. Xiao, Z. Ku, Y. Peng, F. Huang, Y.-B. Cheng and J. Zhong, *Energy Environ. Sci.*, 2017, **10**, 2509–2515.
30 Y. Wang, H. Qu, C. Zhang and Q. Chen, *Sci. Rep.*, 2019, **9**, 459.
31 G. Liu, X. Xi, R. Chen, L. Chen and G. Chen, *J. Renewable Sustainable Energy*, 2018, **10**, 043702.
32 L. Lin, T. W. Jones, J. T.-W. Wang, A. Cook, N. D. Pham, N. W. Duffy, B. Mihaylov, M. Grigore, K. F. Anderson, B. C. Duck, H. Wang, J. Pu, J. Li, B. Chi and G. J. Wilson, *Small*, 2020, **16**, 1901466.
33 P. Zhu, S. Gu, X. Luo, Y. Gao, S. Li, J. Zhu and H. Tan, *Adv. Energy Mater.*, 2019, **10**, 1903083.
34 J. Wei, F. Guo, X. Wang, K. Xu, M. Lei, Y. Liang, Y. Zhao and D. Xu, *Adv. Mater.*, 2018, **30**, 1805153.
35 S. P. Harvey, Z. Li, J. A. Christians, K. Zhu, J. M. Luther and J. J. Berry, *ACS Appl. Mater. Interfaces*, 2018, **10**, 28541–28552.
36 Y. Liu, M. Lorenz, A. V. Ievlev and O. S. Ovchinnikova, *Adv. Funct. Mater.*, 2020, 2002201.
37 Z. Li, C. Xiao, Y. Yang, S. P. Harvey, D. H. Kim, J. A. Christians, M. Yang, P. Schulz, S. U. Nanayakkara, C.-S. Jiang, J. M. Luther, J. J. Berry, M. C. Beard, M. M. Al-Jassima and K. Zhu, *Energy Environ. Sci.*, 2017, **10**, 1234–1242.
38 T. Singh, S. Öz, A. Sasinska, R. Frohnhoven, S. Mathur and T. Miyasaka, *Adv. Funct. Mater.*, 2018, **28**, 1706287.
39 S.-G. Kim, C. Li, A. Guerrero, J.-M. Yang, Y. Zhong, J. Bisquert, S. Huettner and N.-G. Park, *J. Mater. Chem. A*, 2019, **7**, 18807–18815.
40 X. Yin, J. Han, Y. Zhou, Y. Gu, M. Tai, H. Nan, Y. Zhou, J. Li and H. Lin, *J. Mater. Chem. A*, 2019, **7**, 5666–5676.
41 G. Ferraresi, C. Villevieille, I. Czekaj, M. Horisberger, P. Novák and M. E. Kazzi, *ACS Appl. Mater. Interfaces*, 2018, **10**, 8712–8720.
42 M. Namatame, M. Yabusaki, T. Watanabe, Y. Ogomi, S. Hayase and K. Marumoto, *Appl. Phys. Lett.*, 2017, **110**, 123904.
43 M.-C. Jung, S. R. Raga, L. K. Ono and Y. Qi, *Sci. Rep.*, 2015, **5**, 9863.
44 https://github.com/cahlang/2DDriftDi.
45 V. M. L. Corre, M. Stolterfoht, L. P. n. Toro, M. Feuerstein, C. Wolff, L. n. Gil-Escrig, H. J. Bolink, D. Neher and L. J. A. Koster, *ACS Appl. Energy Mater.*, 2019, **2**, 6280–6287.
46 O. J. Sandberg, J. Kurpiers, M. Stolterfoht, D. Neher, P. Meredith, S. Shoaee and A. Armin, *Adv. Mater. Interfaces*, 2020, 2000041.